

Electromagnetic Shielding of Monolayer MXene Assemblies

Taeyeong Yun, Hyerim Kim, Aamir Iqbal, Yong Soo Cho, Gang San Lee, Myung-Ki Kim, Seon Joon Kim, Daesin Kim, Yury Gogotsi,* Sang Ouk Kim,* and Chong Min Koo*

Miniaturization of electronics demands electromagnetic interference (EMI) shielding of nanoscale dimension. The authors report a systematic exploration of EMI shielding behavior of 2D $\text{Ti}_3\text{C}_2\text{T}_x$ MXene assembled films over a broad range of film thicknesses, monolayer by monolayer. Theoretical models are used to explain the shielding mechanism below skin depth, where multiple reflection becomes significant, along with the surface reflection and bulk absorption of electromagnetic radiation. While a monolayer assembled film offers $\approx 20\%$ shielding of electromagnetic waves, a 24-layer film of ≈ 55 nm thickness demonstrates 99% shielding (20 dB), revealing an extraordinarily large absolute shielding effectiveness (3.89×10^6 dB $\text{cm}^2 \text{g}^{-1}$). This remarkable performance of nanometer-thin solution processable MXene proposes a paradigm shift in shielding of lightweight, portable, and compact next-generation electronic devices.

Proliferation of smart, compact, and highly integrated electronics has led to the growing importance of effective shielding from electromagnetic interference (EMI), which causes malfunctioning of electronics and may be harmful for humans.^[1,2] Moreover, recent advances in the portable and wearable electronics require EMI shielding materials with easy processability, lightweight, minimal thickness, flexibility, transparency, and excellent shielding efficiency.^[3–6] MXenes, a large class of 2D carbides, nitrides, and carbonitrides, have shown great promise for lightweight EMI shielding due to their metallic conductivity, strength, flexibility, and solution processability.^[1,7] However, the fundamental mechanism of their outstanding EMI shielding performance is still not well understood, particularly in the nanoscale dimension far smaller than typical electromagnetic field wavelength, such as X-band (8–12 GHz).

We employed ultrathin $\text{Ti}_3\text{C}_2\text{T}_x$ MXene films, obtained by rapid interfacial self-assembly, for the systematic investigation

of layer number dependent EMI shielding behavior in nanometer level thickness. Our interfacial assembly provides large-area densely packed assembled film of low-dimensional materials with a precise atomic level controllability of film thickness.^[8] It is noteworthy that it is difficult to grow a uniform MXene thin film with nanoscale thickness, unlike for graphene and some other 2D materials, via chemical or physical vapor deposition.^[9–12] In this work, Ti_3AlC_2 MAX bulk phase was carefully etched to attain primarily monolayer $\text{Ti}_3\text{C}_2\text{T}_x$ (T_x stands for O, OH, and F surface termination) MXene flakes (see the Supporting Information).^[13] X-ray diffraction (XRD; Figure 1A) of the synthesized MXene detected only (00l) peaks

of MXene, confirming the delamination and good alignment of MXene flakes.^[1,13] A typical monolayer single-crystal flake with hexagonal symmetry shows the lateral size around 5 μm (Figure 1B,C). The obtained high-quality MXene was used for the fabrication of thickness-controlled ultrathin films by interfacial self-assembly (Figure S1, Supporting Information).

Figure 1D shows the atomic force microscopy (AFM) image of a highly uniform assembled MXene film recovered onto a Si substrate with high surface coverage. Partial overlaps among neighboring flakes mediate the integrity over the large-area film and yield the high uniformity and dense packing of assembled film, resulting in the single- to quadruple-sheet thickness, as shown in TEM and AFM images (Figure 1E and Figure S2, Supporting Information). Noticeably, our interfacial assembly ensures the monolayer nature of original $\text{Ti}_3\text{C}_2\text{T}_x$ flakes over the large part of the film (Figure 1F and Figure S3, Supporting Information).^[14] Statistical evaluation by AFM showed that the average thickness of

Dr. T. Yun, G. S. Lee, Prof. S. O. Kim
National Creative Research Initiative Centre for Multi-Dimensional
Directed Nanoscale Assembly
Department of Materials Science and Engineering
KAIST Institute for Nanocentury
Daejeon 34141, Korea
E-mail: sangouk.kim@kaist.ac.kr

H. Kim, A. Iqbal, Y. S. Cho, Dr. S. J. Kim, D. Kim, Prof. C. M. Koo
Materials Architecturing Research Centre
Korea Institute of Science and Technology (KIST)
Seoul 02792, Korea
E-mail: koo@kist.re.kr

 The ORCID identification number(s) for the author(s) of this article can be found under <https://doi.org/10.1002/adma.201906769>.

H. Kim, Y. S. Cho, Prof. M.-K. Kim, D. Kim, Prof. C. M. Koo
KU-KIST Graduate School of Converging Science and Technology
Korea University
Seoul 02841, Korea

A. Iqbal, Prof. C. M. Koo
Division of Nano and Information Technology
KIST School

University of Science and Technology
Daejeon 34113, Korea

Dr S. J. Kim, Prof. Y. Gogotsi
Department of Materials Science and Engineering,
and A. J. Drexel Nanomaterials Institute
Drexel University
Philadelphia, PA 19104, USA
E-mail: gogotsi@drexel.edu

DOI: 10.1002/adma.201906769

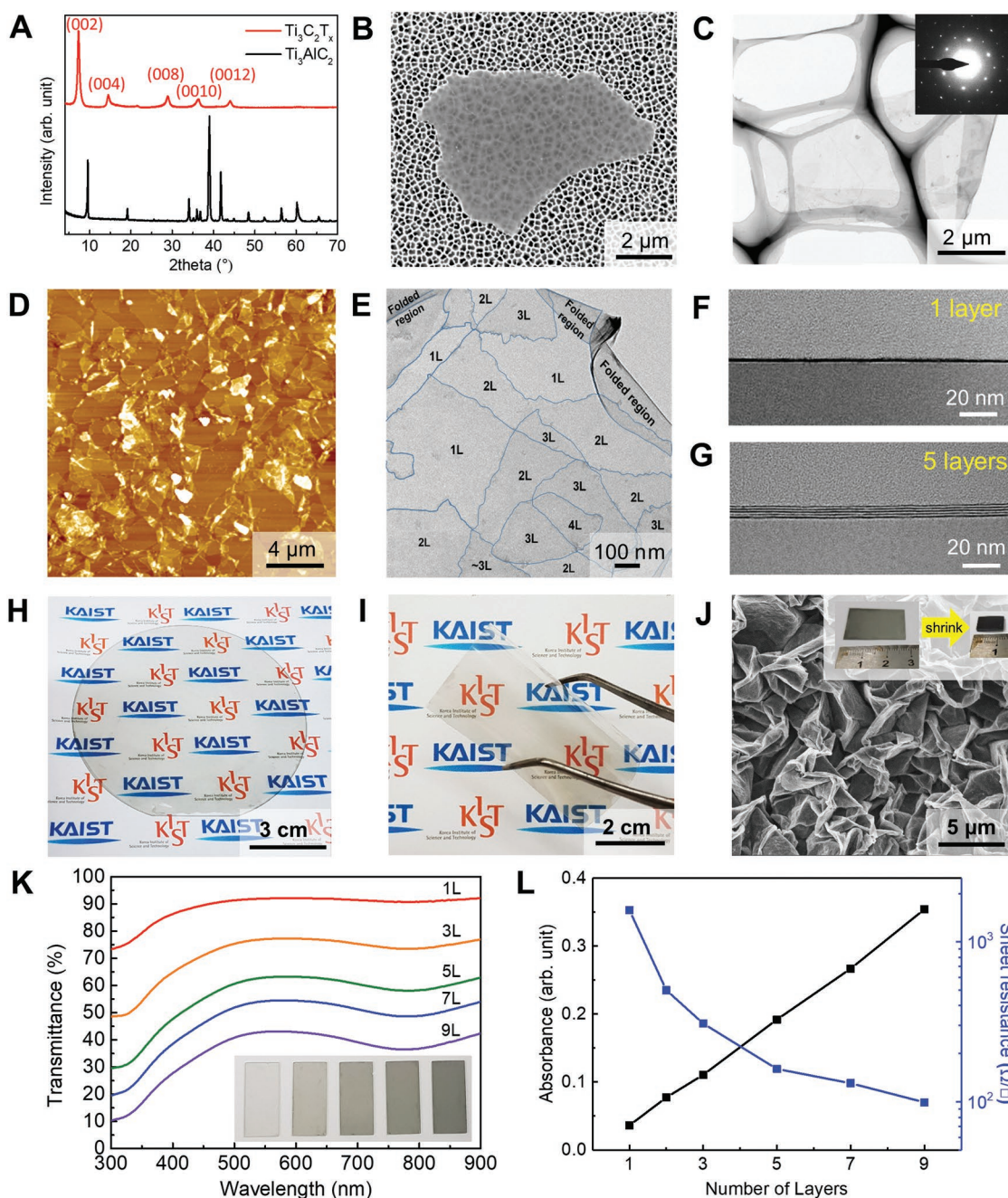


Figure 1. Interfacial self-assembly of MXene films. A) XRD patterns of Ti_3AlC_2 and $\text{Ti}_3\text{C}_2\text{T}_x$. B, C) SEM and TEM images of exfoliated $\text{Ti}_3\text{C}_2\text{T}_x$ flake, respectively. D, E) AFM and TEM images of a monolayer (1L) assembled MXene film, respectively. F, G) Cross-sectional TEM images of monolayer and 5-layer assembled MXene films, respectively. Optical image of MXene films transferred onto H) 4-in. glass wafer, I) flexible PET film, and J) shrinkable PS film after thermal shrinkage at 150 °C. K) UV-vis transmittance spectra of MXene films at different layer stacking numbers; inset shows optical images of the corresponding films on glass. L) Sheet resistance and optical absorbance at 550 nm for various layer stacking numbers of MXene films.

MXene assembled film was 2.3 nm (Figure S4, Supporting Information). This slight deviation from intrinsic monolayer thickness of MXene (1.3 nm) originates from the unavoidable imperfect exfoliation as well as partial edge overlaps among neighboring flakes, which is close to the thickness of two single $\text{Ti}_3\text{C}_2\text{T}_x$ layers prepared by the sequential stacking of multiple assembled layers (see the 5-layer [5L] MXene assembled film in Figure 1G).

Figures 1H,I show the MXene films collected on a 4-in. glass wafer and flexible polyethylene terephthalate (PET) substrate, respectively. Highly flexible MXene films exhibit a strong adhesion to the underlying substrates. Figure 1J shows the film transferred onto a shrinkable polystyrene film before and after thermal shrinkage. Even after the significant thermal shrinkage of the supporting polymer, 3D crumpled MXene film

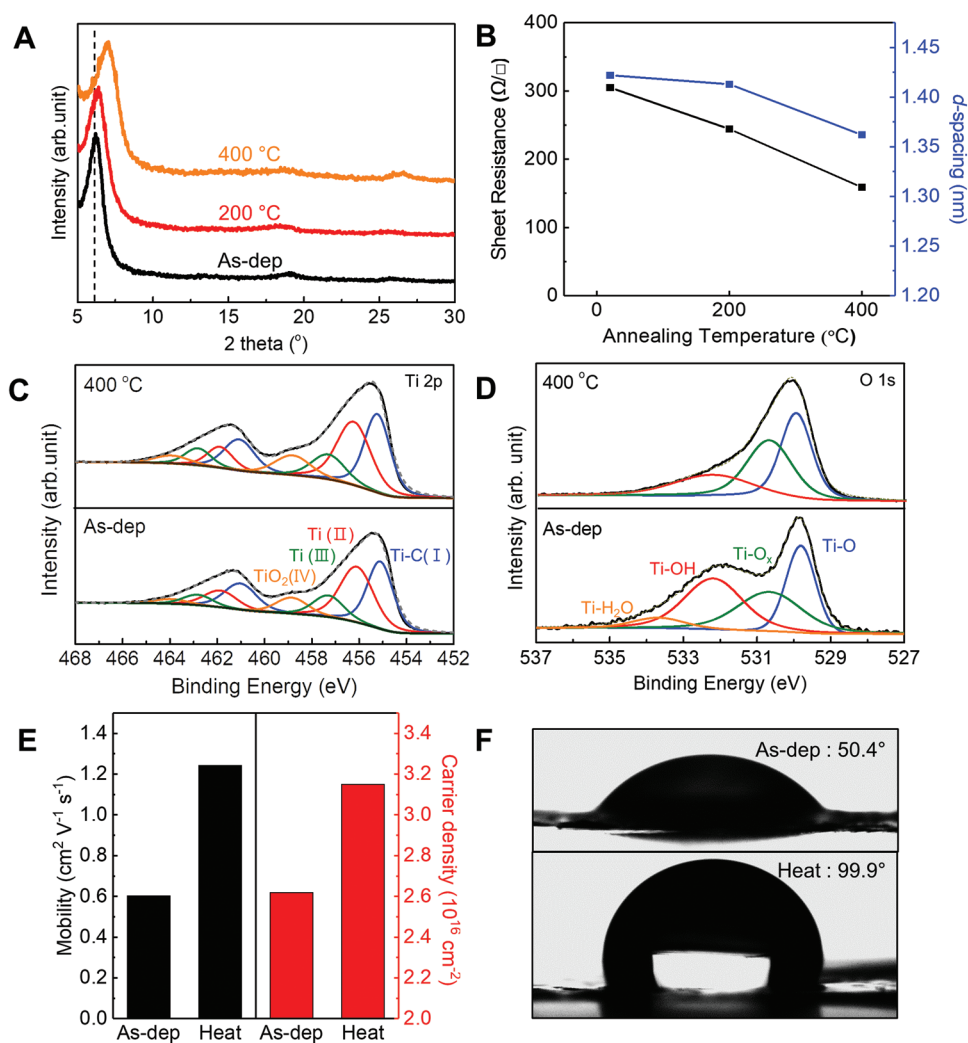


Figure 2. Heat treatment effect on MXene films. A) XRD patterns of 3L MXene films annealed at various temperatures (As-dep stands for as-deposited). B) Sheet resistance and *d*-spacing evolutions of 3L MXene films at various annealing temperatures. XPS spectra of C) Ti 2p and D) O 1s of MXene film before and after 400 °C annealing. E) Charge carrier mobility and density of 3L MXene films before (left) and after (right) thermal annealing. F) Water contact angle measurements of MXene film before (top) and after (bottom) thermal annealing.

retains the tight adhesion to the underlying substrate without delamination (inset of Figure 1)).^[15] Given the high uniformity of the assembled MXene film, the required thickness can be precisely controlled by sequential stacking. Figure 1K shows the optical transmittance of multilayer MXene films collected on a glass substrate. One layer (1L) of assembled film exhibits a transmittance of 90% at a wavelength of 550 nm.^[16] Transmittance gradually decreases with the number of stacked layers, but still remains at 45% for the 9-layer (9L) film. The absorbance (at 550 nm) increases linearly with the number of stacked layers, ensuring the control of film thickness with ≈ 2 nm accuracy (Figure 1L and Figure S5, Supporting Information). Sheet resistance of MXene films is also tunable (Figure 1L). Monolayer (1L) film has a sheet resistance of 1500 Ω/\square , which gradually decreases with the stacking number. This control of MXene film thickness with a nanometer level precision offers a unique opportunity to unveil the intrinsic material properties at the nanoscale thicknesses.

Thermal treatment significantly influences the physical properties of assembled MXene films. **Figure 2A** shows the XRD of 3L MXene films annealed up to 400 °C for 1 h under Ar atmosphere. Oxidation of $\text{Ti}_3\text{C}_2\text{T}_x$ was observed after heating above 600 °C due to removal of surface functional groups and exposure of Ti atoms to air after opening the furnace (Figure S6, Supporting Information). Before thermal treatment, a strong and sharp (002) plane peak was detected, despite the few-nanometers thickness, verifying good alignment of MXene nanosheets. After thermal treatment at 400 °C, the (002) peak of the 3L film upshifted from 6.21° to 6.48°, indicating an interlayer spacing reduction from 1.42 to 1.36 nm (Figure 2B). Its sheet resistance also decreased from 300 to 150 Ω/\square after thermal treatment, while a 1L assembled film went from 1500 to 1056 Ω/\square .

X-ray photoelectron spectroscopy (XPS) survey spectra before thermal treatment (Figure S7, Supporting Information) exhibit sharp peaks for F, O, Ti, and C elements, which originate

from the titanium carbide structure of $\text{Ti}_3\text{C}_2\text{T}_x$ and its surface terminations. Ti 2p peaks (Figure 2C) hardly change even after 400 °C annealing and show four deconvoluted components (Ti-C(I), Ti(II), Ti(III), TiO_2 (IV)) in the form of doublets separated by ≈ 5.8 eV.^[17] Interestingly, the TiO_2 peak (at 458.5 eV) do not grow during thermal treatment, revealing the high oxidation resistance of the film. By contrast, O 1s peaks show a significant change after thermal treatment (Figure 2D). Initially, there are four deconvoluted peaks corresponding to the surface functional groups including –OH, –O, and trapped water molecules, which are inevitably formed during the chemical etching of parental Ti_3AlC_2 . After thermal treatment, peak intensities for Ti-OH and Ti- H_2O are significantly reduced, confirming that reduction in gallery spacing between MXene layers upon thermal treatment is not due to the phase transformation to TiO_2 or oxidation of MXene, but due to the removal of intercalants, such as absorbed H_2O and partial loss of surface terminations such as –OH, –F, and –O.^[4,18]

Hall effect measurements compare the carrier density and mobility of MXene films before and after thermal treatment (Figure 2E). The major charge carriers in MXene are electrons.^[17] Thermal treatment increases the carrier mobility from 0.6 to 1.25 $\text{cm}^2 \text{V}^{-1} \text{s}^{-1}$ and carrier density from 2.6×10^{16} to $3.2 \times 10^{16} \text{ cm}^{-2}$.^[17,19] These enhancements are also attributed to the removal of surface terminations, generally known as electron scattering sites in 2D materials.^[20] The removal of hydrophilic terminal groups can also be visualized by water contact angle measurement (Figure 2F). As-assembled MXene film showed a moderately hydrophilic nature with a contact angle of 50.4°, increasing to 99.9° after thermal treatment.^[4]

Figure 3A,B present the total EMI shielding effectiveness (SE_T) of MXene films before and after 400 °C annealing, respectively, over a frequency range of 8.2–12.4 GHz (X-band). Shielding by reflection (SE_R) and absorption (SE_A) was also obtained (see Figure S8, Supporting Information). Monolayer (1L) MXene film has an SE_T of 1 dB at 8.2 GHz, offering $\approx 20\%$ shielding of incident EM waves. The SE_T rapidly increases with stack number and reaches 10 dB at 9L film to attenuate 90% of EM wave. Obviously, thermal treatment greatly improves the SE_T while reducing sheet resistance. A 5L film reaches ≈ 10 dB after thermal treatment, while a 24L film goes to ≈ 20 dB, satisfying the commercial requirement for consumer electronics (99% attenuation).^[1] In Figure 3C, increasing rate of SE_T for the thermally treated films is also much higher over untreated films.

Figure 3D shows the components of SE_T , SE_R , and SE_A of thermally treated MXene films as a function of film thickness at 8.2 GHz. Interestingly, electrically thin MXene films also show a strong absorption-dominant shielding behavior ($\text{SE}_A > \text{SE}_R$), similar to the electrically thick MXene films.^[1,4] Generally, the term “electrically thin” is used for the thickness below skin depth and vice versa. At skin depth, the intensity of EM wave falls to $1/e$ of the incident wave, which is given by $\delta = \sqrt{1/\pi\sigma\mu f}$, where σ , μ , and f are conductivity, permeability, and frequency, respectively.^[21,22] In the case of our highly conductive $\text{Ti}_3\text{C}_2\text{T}_x$ MXene with the electrical conductivity of 5000 S cm^{-1} , the skin depth is 7.86 μm at 8.2 GHz.

Figure 3E shows the variation of SE_T over electrically thin to thick range (from 2.3 nm to 45 μm) and the comparison with

theoretical calculations.^[1,21–24] For a systematic understanding of shielding mechanism, two different models, including Simon's formalism^[24] and transfer matrix method,^[22,23] are introduced (see Supporting Information). While the former only considers reflection (SE_R) and absorption (SE_A), the latter includes all the possible shielding mechanisms, including multiple reflections (SE_{MR}), in addition to SE_R and SE_A . As we previously reported, micrometer-thick MXene films show a linear increment of SE_T for the thickness over 1.5 μm , consistent with Simon's formula (blue line) (Figure 3E).^[1] However, Simon's formula fails to fit the experimental results below skin depth (7.86 μm). The SE_T values of electrically thin MXene films are no longer linearly related to film thickness, but rather follow the prediction from the transfer matrix method (red line).^[22,23,25] Such a deviation is also prominent for SE_R (Figure S9A, Supporting Information).

While Simon's formula (Equation (8), Supporting Information) suggests that the SE_R values at constant conductivity (σ) should be independent of the thickness of shield, transfer matrix method presents a strong dependence on the thickness. It also highlights the significant role of multiple reflections at the low thickness.^[21] A nonlinear relationship between SE_A and film thickness also supports this phenomenon below skin depth (Figure S9B, Supporting Information).^[1,24]

Notably, while the electric field of transverse electric (TE) mode waves is parallel to the plane of MXene film, the interference effect hardly occurs during multiple reflections within a very thin film because the total propagation pathway of EM waves is much shorter than the wavelength. By contrast, even long-wavelength microwaves can interact with the nanometer-thin MXene film, since the electric field of EM waves is parallel to the plane of MXene thin film with infinite surface area. Therefore, EM waves directed surface normal to the MXene film plane can undergo not only reflection and absorption but also significant multiple reflections even in the nanometer-thick films.^[23,25]

Under the multiple reflections, reflected waves from the backside interface undergo additional reflections and absorptions inside the shielding material over and over, until they are either transmitted or completely attenuated (Figure S10, Supporting Information).^[21] Such a mechanism results in lower SE_T , higher SE_A , and lower SE_R contributions, which is in agreement with our experiment over the entire thickness range. This consistency also confirms that our self-assembled films possess excellent homogeneity and uniformity, even at nanometer scale (Figure S9C, Supporting Information). In addition, surface terminations on the MXene films aligned in the direction of applied electric field undergo polarization, resulting in attenuation by polarization losses.^[26] This surface functionality effect should be significant in the highly exfoliated MXene flakes with large surface area and can contribute to the enhancement of SE_A . Moreover, gallery spacing between the stacked MXene layers may form capacitor-like structures under electromagnetic field and lead to capacitive energy dissipation.^[27] Inter-flake electron hopping among the assembled MXene flakes can also partially add up in attenuating energy of EM waves.^[26]

EMI shielding effectiveness (EMI SE) of the assembled MXene films was compared with that of electrochemically exfoliated graphene (EG) films prepared by a similar interfacial self-assembly, spin-coated MXene and reduced graphene oxide (rGO) films, and E-beam evaporated gold (Au) films

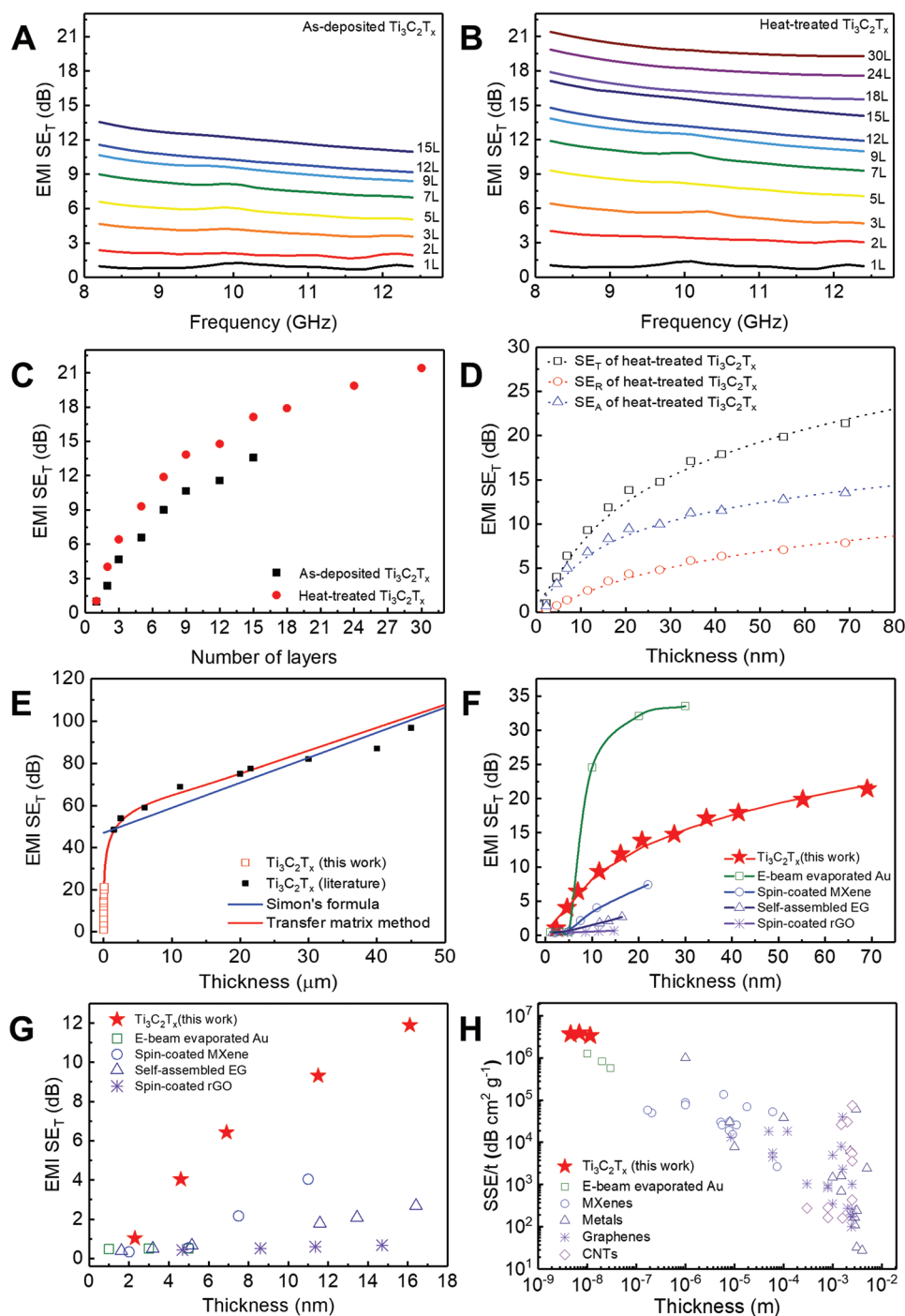


Figure 3. EMI SE of MXene films with various numbers of layers. A,B) EMI SE_T values in X-band range before and after 400 °C annealing, respectively. C) EMI SE_T values for 8.2 GHz before (black) and after (red) 400 °C annealing. D) Experimental EMI SE_T , SE_R , and SE_A values of 400 °C annealed films. E) Comparison of EMI SE_T values between simulation (red: transfer matrix method, blue: Simon's formula) and experiment (red open dots: the present study, black dots: Shahzad's report^[1]). F) Comparison of EMI SE as a function of thickness for various shielding materials. G) EMI SE_T values for various shielding materials under 20 nm thickness; enlarged Figure 1F to highlight the behavior of thin films. H) SSE/t as a function of thickness for different high-performance shielding materials.

with similar thicknesses (Figure 3F). Figure 3G magnifies the lower thickness region. Interfacially assembled MXene films reveal much larger EMI SE_T values than EG and rGO films at the comparable film thickness principally due to the

conductivity difference (MXene films: $\approx 5000 \text{ S cm}^{-1}$, thermally reduced EG and rGO films $\approx 200 \text{ S cm}^{-1}$).^[28] The ideal electrical conductivity of graphene relying on high carrier mobility is hard to exploit for EMI shielding, particularly in the practical

solution processed films with unavoidable defects and distortions. By contrast, the larger carrier density in MXene ensures a reliable EMI shielding performance. Self-assembled MXene films also reveal significantly larger EMI SE_T over spin-coated MXene films, particularly at the low thickness region, where the lower uniformity of spin-coated MXene films affects the electrical conductivity and shielding efficiency. Most interestingly, the assembled MXene films have higher EMI SE_T than E-beam evaporated gold film below 5 nm thickness because of lower uniformity of the gold film. Additionally, a strong surface scattering at gold film thinner than electron mean free path (37.7 nm) could also contribute to the inferior shielding performance.^[29,30]

Absolute shielding effectiveness (SSE/t) values of the assembled MXene films are compared with literature data in Figure 3H. The SSE/t value is calculated from the normalization of EMI SE_T with respect to density and thickness for a comparison at the same areal mass density. While large SSE/t values are highly desirable for lightweight shielding applications,^[1,4] the self-assembled MXene films outperform all the existing state-of-the-art synthetic materials, leaving behind even highly conductive metals like gold with higher density. For 3L MXene, the value reaches $2.83 \times 10^6 \text{ dB cm}^2 \text{ g}^{-1}$ (≈ 3 million) and further improves to $3.89 \times 10^6 \text{ dB cm}^2 \text{ g}^{-1}$ after thermal treatment, the largest value ever reported thus far (exact values for other materials are listed in Table S1, Supporting Information).

This work manifests the outstanding EMI shielding performance of $\text{Ti}_3\text{C}_2\text{T}_x$ MXene and can lead to a paradigm change in protection of lightweight, portable, and flexible next-generation electronics. Nanometer-thin films of titanium carbide and, potentially, other metallic MXenes, may be able to replace heavy metal foils or millimeter-thick carbon composites. Our theoretical analysis shows the importance of 2D nature of the metallic material for achieving multiple reflections and strong attenuation of electromagnetic waves. Also, considering that the conductivity of micron-thick films of $\text{Ti}_3\text{C}_2\text{T}_x$ already exceeds $10\,000 \text{ S cm}^{-1}$ and further improvements are expected, more than 30 MXenes are already available and dozens more underway, there are exciting opportunities for further control of microwaves with ultrathin films of metallic 2D carbides and nitrides produced by scalable solution processing.^[31,32]

Experimental Section

Materials: Ti_3AlC_2 MAX powder with a particle size of 40 μm was purchased from Carbon-Ukraine Ltd. (Ukraine). Lithium fluoride (LiF, 98.5%) was acquired from Alfa Aesar (USA). Hydrochloric acid (HCl, 37%) and ethyl acetate (EA, 99%) were purchased from Sigma-Aldrich (USA). All chemicals were used as received.

Synthesis of Exfoliated MXene Flakes: $\text{Ti}_3\text{C}_2\text{T}_x$ was synthesized from the parent Ti_3AlC_2 powder using the minimally intensive layer delamination method.^[13] LiF (4.8 g) was added to 9 M HCl solution (60 mL) with stirring. Ti_3AlC_2 powder (3 g) was added slowly into the well-dissolved LiF solution to avoid the side reactions caused by an abrupt temperature increase (exothermic etching reaction), and continuously stirred at 35 $^\circ\text{C}$ for 24 h. Afterward, the etched sample was washed with deionized water and centrifuged repeatedly at 3500 rpm until the $\text{Ti}_3\text{C}_2\text{T}_x$ supernatant turned dark-green at around pH 5. The dispersed solution was centrifuged at 3500 rpm for an hour to obtain a stable supernatant and separated into $\text{Ti}_3\text{C}_2\text{T}_x$ and Ti_3AlC_2 . To obtain uniformly delaminated MXene flakes, exfoliated $\text{Ti}_3\text{C}_2\text{T}_x$ solution was

bath sonicated in an ice bath for an hour. Subsequently, the solution was centrifuged at 5000 rpm for 30 min, and the collected supernatant with the concentration of 3–5 mg mL^{-1} was used for the interfacial self-assembly of MXene films.

Fabrication of Assembled MXene Thin Films with Nanometers Level Thickness Precision: Nanometer-thin MXene films were fabricated by interfacial self-assembly technique of exfoliated 2D flakes in a dilute aqueous colloidal solution, as illustrated in Figure S1, Supporting Information.^[8,33,34] For interfacial self-assembly, exfoliated MXene solution (40 μL , 3 mg mL^{-1}) was added to distilled water (40 mL). To screen the surface negative charge of MXene flakes, HNO_3 (1 mL, 1 M) was added to the diluted MXene solution. By adding ethyl acetate (EA, 2 mL) dropwise onto the surface of diluted MXene solution, a strong vertical convection, called Rayleigh–Bénard convection, is induced over the entire dispersion volume by the endothermal evaporation of EA. This vertical convection delivers the dissolved MXene flakes from the entire dispersion volume to the air–water interface. The lateral self-assembly of the floated MXene flakes into a densely packed uniform MXene thin film is driven by the Marangoni effect, derived from the surface tension difference between water and EA.^[8] Finally, the assembled nanometer-thick MXene film is directly transferred onto any substrate of choice, such as glass or polymer film, and multilayer films are prepared containing up to 15-layers by sequential stacking of the multiple assembled films. In more detail, the substrate was immersed in water and the floating MXene film was coated by scooping onto a substrate. Then, the coated film was dried vertically in air. The multi-stacked films were fabricated by a repetitive coating process on a single substrate with a desired number of stacking cycles.

Self-assembled EG films, spin-coated rGO films, spin-coated MXene films, and E-beam evaporated Au films were prepared as follows. Fabrication of self-assembled EG film followed from a previous work.^[8] EG were suspended in NMP solution with a concentration of 0.5 mg mL^{-1} , which was mixed with deionized water. By adding EA dropwise into the surface of the graphene suspension, the EG film was assembled and transferred on the target substrate. To obtain multilayered EG films, sequential stacking was conducted like multilayer MXene. Self-assembled EG films were thermally annealed at 600 $^\circ\text{C}$ for 1 h under argon atmosphere to increase the conductivity before EMI shielding measurements. Spin-coated rGO film was prepared by spin-casting of graphene oxide (GO) solution and following thermal annealing. GO solution (3 mg mL^{-1}) was spin-cast at 3000 rpm. The thickness of the GO film was controlled with the repetitive spin-coating steps. The spin-coated rGO film was prepared via thermal annealing of the spin-cast GO film at 600 $^\circ\text{C}$ for 1 h under argon atmosphere. Spin-coated MXene film was fabricated with 2000 rpm. To fabricate films with different thicknesses, the various concentrations of 0.5, 1, 3, 5, and 7 mg mL^{-1} MXene solutions were spin-cast. Au thin film was deposited on the target substrate with 0.2–0.5 \AA sec^{-1} by using E-beam evaporator.

Materials Characterization: Scanning electron microscope (SEM) measurements were performed using Hitachi S-4800 (Hitachi, Japan). The assembled MXene film was directly transferred onto a gold TEM grid (G200-Au from Gilder Grids, UK) with tweezers and dried under ambient atmosphere.^[8] High-resolution transmission electron microscopy images and the elemental mapping of MXene were acquired using Talos F200X TEM (FEI company, USA) with 200 kV accelerating voltage. The chemical composition was analyzed using XPS, (Thermo VG Scientific, Sigma Probe, USA). XRD was measured by a D8 diffractometer with Cu-K α radiation (40 kV and 44 mA), a 2θ range of 4° – 70° , a scanning step of 0.02° , a time step of 0.5 s, and a window slit of $10 \times 10 \text{ mm}^2$. The UV–vis absorbance spectra were measured using a UV–vis spectrophotometer (Shimadzu, UV-2600, Japan). AFM measurements were obtained using a Multimode 8 (Bruker, USA) with a tapping mode. Sheet resistance was measured using a 4-point probe (MCP-TP06P PSP) with a Loresta-GP meter (MCP-T610 model, Mitsubishi Chemical, Japan). The distance among the pin of the probes was 1.5 mm, and the voltage at the open terminal was set as 10 V. The charge carrier density and mobility were measured by Hall effect measurement (8404 HMS,

Lakeshore, USA). The contact angle measurement was performed using contact angle measuring equipment (GSS, SurfaceTech Co., Ltd., Korea).

Electromagnetic Interference Shielding Measurements: EMI shielding measurements of the films were carried out in a WR-90 rectangular TE10 mode waveguide using a 2-port network analyzer (ENA5071C, Agilent Technologies, USA) in the X-band frequency range (8.2–12.4 GHz). In the transverse electric TE10 mode waveguide, the electric field of the wave is perpendicular to the direction of wave propagation. The standard procedure was performed for calibrating the equipment using short offset, short, and load on both ports, 1 and 2. The nanometer-thick MXene film was coated on the glass wafer with the rectangular shape dimension (25.4 mm × 12.7 mm × 0.5 mm).

Theoretical Calculations of EMI Shielding: EMI SE, measured in decibels (dB), is the ability of a material to attenuate (shield) the energy of the incident EM waves. Generally, this phenomenon occurs due to three different shielding mechanisms; namely, shielding due to reflection (SE_R), absorption (SE_A), and multiple reflections (SE_{MR}), as illustrated in Figure S10, Supporting Information.^[35] An incident EM wave (E_i) was partially reflected (E_{r1}) and partially refracted from the front shield surface. While the refracted EM wave (E_{t1}) propagated inside the shield, some of EM wave energy was absorbed due to the attenuation property of a lossy shield. The EM wave that survived to the backside surface experienced partial reflection (E_{r2}) and transmission (E_{t2}) at the backside surface again, and the reflected EM wave from backside interface causes multiple reflections. The reflected EM waves were partially reflected, absorbed, and transmitted repeatedly during forward and backward multiple reflections (E^+ and E^- ; respectively) until all the EM energy was attenuated completely.

Thus, the total EMI SE (SE_T) can be written as

$$SE_T = SE_R + SE_A + SE_{MR} \quad (1)$$

First of all, we can calculate reflection (R) and transmission (T) values using their coefficients (r and t , respectively) obtained from the vector network analyzer in the form of scattering parameters (S_{11} , S_{22} , S_{12} , and S_{21} , here $r = S_{11} = S_{22}$ and $t = S_{12} = S_{21}$) as

$$R = |r|^2 = |S_{11}|^2 \quad (2)$$

$$T = |t|^2 = |S_{12}|^2 \quad (3)$$

SE_T , SE_R , and SE_A are calculated from the measured reflection (R) and transmission (T) as follows

$$SE_T = 10 \log\left(\frac{1}{T}\right) = 10 \log\left(\frac{1}{|t|^2}\right) \quad (4)$$

$$SE_R = 10 \log\left(\frac{1}{1-R}\right) = 10 \log\left(\frac{1}{1-|r|^2}\right) \quad (5)$$

$$SE_A = 10 \log\left(\frac{1-R}{T}\right) = 10 \log\left(\frac{1-|r|^2}{|t|^2}\right) \quad (6)$$

Assuming the EM waves propagate in a nonmagnetic and highly conducting medium, the Fresnel formula provides us with the equation dealing with reflection, absorption, and multiple reflections as^[21,36,37]

$$SE_T = 10 \log\left(\frac{1}{T}\right) = 10 \log\left(\frac{E_i}{E_t}\right)^2 = 20 \log\left[\frac{(1+N)^2}{4N} e^{-kd} \left[1 - \frac{(1-N)^2}{(1+N)^2} e^{2ikd}\right]\right] \quad (7)$$

where E_i and E_t are the intensities of the incident and transmitted electric field of the EM waves, respectively; d is the thickness, and N is the complex

refractive index of the shield, while k is the imaginary part of refractive index.

The complex refractive index of the MXene (N_m) is set to $N_m = \sqrt{\frac{\sigma}{2\omega\epsilon_0}}(1+i)$, since MXene has a high conductivity of 5000–10 000 S cm⁻¹.^[38]

SE_R , SE_A , and SE_{MR} are expressed as

$$SE_R = 20 \log\left(\frac{(1+N)^2}{4|N|}\right) = 50 + 10 \log\left(\frac{\sigma}{f}\right) \quad (8)$$

$$SE_A = 20 \log e^{-kd} = 20 \log e^{\alpha d} = 8.686 \alpha d = 1.7d\sqrt{\sigma f} \quad (9)$$

$$SE_{MR} = 20 \log\left|1 - e^{(2ikd)} \frac{(1-N)^2}{(1+N)^2}\right| \quad (10)$$

In Equation (9), α is the attenuation constant, which causes the EM wave signal to attenuate along a transmission line.

Simon's Formalism: Simon's formula is very simple and versatile to use for calculating SE_T of electrically thick materials. It neglects the multiple reflections effect. Electrically thick conductive materials have the thickness higher than the skin depth δ .^[21] The skin depth is the thickness by which the intensity of the EM wave falls to $1/e$ of the incident wave's intensity and is given by $\delta = \frac{1}{\alpha} = \sqrt{1/\pi\sigma\mu f}$, where σ and f are conductivity and frequency, respectively.^[21] When the thickness is much larger than skin depth or the SE_T value is larger than 15 dB,^[1] multiple reflections' effect is negligible. Therefore, Simon's formula is derived by the sum of SE_R (Equation (8)) and SE_A (Equation (9)). Therefore, total EMI SE_T can be represented by an equation as follows.^[1,24]

$$SE_T = 50 + 10 \log\left(\frac{\sigma}{f}\right) + 1.7d\sqrt{\sigma f} \quad (11)$$

The above equation is named Simon's formalism, where σ is the electrical conductivity (S cm⁻¹), f is the frequency (MHz), and d is the thickness of the shield (cm). The first two terms of the equation represent shielding due to reflection, while the third term indicates shielding due to absorption.

However, in this work, the electrically thin MXene films were analyzed with their thickness values being much lower than the MXene's calculated skin depth of 7.86 μ m, (at $\sigma = 5000$ S cm⁻¹ and $f = 8.2$ GHz), where the role of multiple reflections cannot be neglected. Hence, the transfer matrix method was applied to account for multiple reflections in multilayer assembled MXene films.

Transfer Matrix Method: To calculate the EMI SE_T , SE_R , and SE_A for a thin MXene layer, the transfer matrix method was employed.^[22,23] The transfer matrix method is a way to get a complete analytical solution for the calculation of transmission, reflection, and absorption of EM waves propagating through a 2D infinite plane interface and a layer of a given thickness. This method even allows the calculation of exact electromagnetic boundary conditions at each interface of a very thin 2D infinite layer that is much smaller than the wavelength of incident wave. It thoroughly considers the multiple reflections. The transfer equation for the propagation through a thin layer can be expressed by three matrices as follows.

$$\begin{pmatrix} E_i^+ \\ E_i^- \end{pmatrix} = M_{1(N_m, N_w)} \cdot M_{2(N_m, d)} \cdot M_{1(N_w, N_m)} \begin{pmatrix} E_t^+ \\ E_t^- \end{pmatrix} = \begin{pmatrix} a & b \\ c & d \end{pmatrix} \begin{pmatrix} E_i^+ \\ E_i^- \end{pmatrix} \quad (12)$$

where M_1 and M_2 are the transfer matrices for the propagation through an interface and propagation within a lossy shielding layer, respectively. Accordingly, $M_{1(N_w, N_m)}$, $M_{2(N_m, d)}$, and $M_{1(N_m, N_w)}$ represent the matrices for the propagation through an interface from air to MXene, the propagation within the MXene layer with thickness d , and the propagation through an interface from MXene to air, respectively. E_i and E_t are the electric field amplitudes of the incident and transmitted electromagnetic waves, respectively, and E^+ and E^- represent the electric

field amplitudes of the forward and backward electromagnetic waves in a medium, respectively.

In the homogeneous and isotropic media, the matrices M_1 and M_2 are expressed as

$$M_{1(N_i, N_j)} = \frac{1}{t_{ij}} \begin{pmatrix} 1 & -r_{ij} \\ -r_{ij} & 1 \end{pmatrix} \text{ and } M_{2(N, d)} = \begin{pmatrix} \Phi^{-1} & 0 \\ 0 & \Phi \end{pmatrix} \quad (13)$$

respectively. Here, r and t are the complex amplitude reflection and transmission Fresnel coefficients, respectively. For the TE modes, r and t are represented by

$$r_{ij} = \frac{N_i \cos \theta_i - N_j \cos \theta_j}{N_i \cos \theta_i + N_j \cos \theta_j} \text{ and } t_{ij} = \frac{2N_i \cos \theta_i}{N_i \cos \theta_i + N_j \cos \theta_j} \quad (14)$$

respectively; where $N_{i \text{ or } j}$ is the complex refractive index of the layer i or j , and $\theta_{i \text{ or } j}$ is the propagation angle in the layer i or j . Φ is represented by $\Phi = e^{-i \frac{2\pi}{\lambda} Nd}$, where d is the thickness of the medium and λ is the wavelength in free space.

In the calculations, $\cos \theta_{\text{air}}$ is defined as $\cos \theta_{\text{air}} = \sqrt{1 - \left(\frac{\pi}{T}\right)^2} / k_0^2$ with the assumption of TE₁₀ mode, where l is the broadside length of the rectangular waveguide.^[36] Moreover, $\cos \theta_m$ is equal to $N_{\text{air}} \cos \theta_{\text{air}} / N_m$ according to Snell's law. The complex refractive indices of MXene (N_m) and air (N_{air}) were set to $N_m = \sqrt{\frac{\sigma}{2\omega_0}}(1+i)$, and $N_{\text{air}} = 1$, respectively, where σ is the conductivity of the MXene.

From Equation (12), the reflection and transmission coefficients are expressed by

$$R = -\frac{c}{d} \text{ and } T = a - \frac{bc}{d} \quad (15)$$

respectively.

Therefore, using Equation (15), SE_T , SE_R , and SE_A can be calculated using the following relations

$$SE_T = 10 \log \left(\frac{1}{T} \right) = 10 \log \left(\frac{1}{|t|^2} \right) \quad (16)$$

$$SE_R = 10 \log \left(\frac{1}{1-R} \right) = 10 \log \left(\frac{1}{1-|r|^2} \right) \quad (17)$$

$$SE_A = SE_T - SE_R \quad (18)$$

Theoretically calculated values based on the transfer matrix method and Simon's formula were obtained with the assumption of 5000 S cm⁻¹ electrical conductivity of MXene films.

Calculation of Absolute Shielding Effectiveness: Highly conductive metal foils and films show excellent shielding efficiency at the micrometer thickness. However, their large specific weight limits their applications in numerous areas like aerospace and telecommunications, where requirement of lightweight is imperative. In contrast, lightweight materials such as aerogels and foam structures exhibit better performance due to lower density, at the expense of occupied volume due to the required large thickness. This means that for real-life applications, efficient shielding materials should exhibit excellent EMI SE at minimal thickness, while simultaneously having a low density. Hence the specific shielding effectiveness (SSE), which considers only density of the material as shown in Equation (19), is not sufficient.^[1] To manage this limitation, a term "absolute shielding effectiveness" (SSE/ t) is defined to take into account the density as well as the thickness of the material. SSE/ t is calculated by dividing EMI SE with the density and thickness, as presented in Equation (20).^[1,39]

$$SSE = \text{EMI SE} / \text{density} = \text{dB cm}^3 \text{ g}^{-1} \quad (19)$$

$$SSE/t = SSE_t = \text{EMI SE} / \text{density} / t = \text{dB cm}^2 \text{ g}^{-1} \quad (20)$$

The SSE/ t well defines the efficiency of the material toward real-life applications, as higher SSE/ t values are needed for modern smart and miniaturized electronic devices. The self-assembled nanometer-thick Ti₃C₂T_x films are potential candidates for these applications in electronic devices for the Internet of Things and other advanced technologies.

Supporting Information

Supporting Information is available from the Wiley Online Library or from the author.

Acknowledgements

The authors would like to thank Dr. Dong-Ho Kim and Ah Ra Kim (KIMS) for assistance in Hall measurements, and Dr. Meikang Han (Drexel University) and Dr. Sangho Cho (KIST) for their helpful comments on the manuscript. A.I. and S.J.K. acknowledge Dr. Babak Anasori and Mr. Mohamed Alhabeb (Drexel University) for their guidance in MXene synthesis. C.M.K. acknowledges Pohang Light Source for assistance in diffraction measurements. This work was financially supported by KIST-KAIST joint research lab (2V05750), KU-KIST research, young fellow, and KIST internal research programs funded by Korea Institute of Science and Technology (KIST). This work was also supported by grants from the Basic Science Research Program (2017R1A2B3006469 and 2019M3D1A2014004) through the National Research Foundation of Korea funded by the Ministry of Science, ICT, and Future Planning, the Fundamental R&D Program (10077545) for Core Technology of Materials and the Industrial Strategic Technology Development Program funded by the Ministry of Trade, Industry & Energy, and Construction Technology Research Project (19SCIP-B146646-02) funded by Ministry of Land, Infrastructure and Transport, Republic of Korea. T.Y., G.S.L. and S.O.K. were partially supported by the National Creative Research Initiative (CRI) Centre for Multi-Dimensional Directed Nanoscale Assembly (2015R1A3A2033061) funded by the National Research Foundation (NRF) of Korea. Collaboration between KIST, KAIST, and Drexel University was supported by the Leading Foreign Research Institute Recruitment Program (NNFC-Drexel-SMU FIRST Nano Co-op Centre, 2015K1A4A3047100) of the National Research Foundation (NRF) of Korea, funded by the Ministry of Science and ICT, Korea.

Conflict of Interest

The authors declare no conflict of interest.

Author Contributions

T.Y., H.K., and A.I. contributed equally to this work. C.M.K. and S.O.K. conceived the idea. T.Y., H.K., G.S.L., Y.S.C. mainly performed the experiments. D.K. helped with the MXene synthesis. M.K.K., C.M.K., and A.I. conducted the theoretical calculations. T.Y., A.I., H.K., G.S.L., C.M.K., and S.O.K. drafted the manuscript, S.J.K. and Y.G. reviewed and shaped the manuscript, and all the authors contributed to editing of the manuscript. C.M.K., S.O.K., and Y.G. supervised the entire work.

Keywords

2D materials, electromagnetic interference shielding, MXene, nanomaterials, self-assembly

Received: October 15, 2019

Revised: November 21, 2019

Published online:

- [1] F. Shahzad, M. Alhabeb, C. B. Hatter, B. Anasori, S. M. Hong, C. M. Koo, Y. Gogotsi, *Science* **2016**, 353, 1137.
- [2] Y. Han, J. Lin, Y. X. Liu, H. Fu, Y. Ma, P. Jin, J. B. Tan, *Sci. Rep.* **2016**, 6, 25601.
- [3] J. Jung, H. Lee, I. Ha, H. Cho, K. K. Kim, J. Kwon, P. Won, S. Hong, S. H. Ko, *ACS Appl. Mater. Interfaces* **2017**, 9, 44609.
- [4] J. Liu, H. B. Zhang, R. H. Sun, Y. F. Liu, Z. S. Liu, A. G. Zhou, Z. Z. Yu, *Adv. Mater.* **2017**, 29, 1702367.
- [5] S. Lin, H. Wang, F. Wu, Q. Wang, X. Bai, D. Zu, J. Song, D. Wang, Z. Liu, Z. Li, N. Tao, K. Huang, M. Lei, B. Li, H. Wu, *NPJ Flexible Electron.* **2019**, 3, 6.
- [6] Z. Chen, C. Xu, C. Ma, W. Ren, H.-M. Cheng, *Adv. Mater.* **2013**, 25, 1296.
- [7] B. Anasori, M. R. Lukatskaya, Y. Gogotsi, *Nat. Rev. Mater.* **2017**, 2, 16098.
- [8] J. Shim, J. M. Yun, T. Yun, P. Kim, K. E. Lee, W. J. Lee, R. Ryoo, D. J. Pine, G. R. Yi, S. O. Kim, *Nano Lett.* **2014**, 14, 1388.
- [9] X. H. Sang, Y. Xie, D. E. Yilmaz, R. Lotfi, M. Alhabeb, A. Ostadhossein, B. Anasori, W. W. Sun, X. F. Li, K. Xiao, P. R. C. Kent, A. C. T. van Duin, Y. Gogotsi, R. R. Unocic, *Nat. Commun.* **2018**, 9, 2266.
- [10] J.-H. Lee, E. K. Lee, W.-J. Joo, Y. Jang, B.-S. Kim, J. Y. Lim, S.-H. Choi, S. J. Ahn, J. R. Ahn, M.-H. Park, C.-W. Yang, B. L. Choi, S.-W. Hwang, D. Whang, *Science* **2014**, 344, 286.
- [11] H. Yu, M. Liao, W. Zhao, G. Liu, X. J. Zhou, Z. Wei, X. Xu, K. Liu, Z. Hu, K. Deng, S. Zhou, J.-A. Shi, L. Gu, C. Shen, T. Zhang, L. Du, L. Xie, J. Zhu, W. Chen, R. Yang, D. Shi, G. Zhang, *ACS Nano* **2017**, 11, 12001.
- [12] J. Halim, M. R. Lukatskaya, K. M. Cook, J. Lu, C. R. Smith, L.-Å. Näslund, S. J. May, L. Hultman, Y. Gogotsi, P. Eklund, M. W. Barsoum, *Chem. Mater.* **2014**, 26, 2374.
- [13] M. Alhabeb, K. Maleski, B. Anasori, P. Lelyukh, L. Clark, S. Sin, Y. Gogotsi, *Chem. Mater.* **2017**, 29, 7633.
- [14] A. D. Dillon, M. J. Ghidui, A. L. Krick, J. Griggs, S. J. May, Y. Gogotsi, M. W. Barsoum, A. T. Fafarman, *Adv. Funct. Mater.* **2016**, 26, 4162.
- [15] J. Y. Kim, J. Lim, H. M. Jin, B. H. Kim, S. J. Jeong, D. S. Choi, D. J. Li, S. O. Kim, *Adv. Mater.* **2016**, 28, 1591.
- [16] C. F. Zhang, B. Anasori, A. Seral-Ascaso, S. H. Park, N. McEvoy, A. Shmeliov, G. S. Duesberg, J. N. Coleman, Y. Gogotsi, V. Nicolosi, *Adv. Mater.* **2017**, 29, 1702678.
- [17] A. Lipatov, M. Alhabeb, M. R. Lukatskaya, A. Boson, Y. Gogotsi, A. Sinitskii, *Adv. Electron. Mater.* **2016**, 2, 1600255.
- [18] J. L. Hart, K. Hantanasirisakul, A. C. Lang, B. Anasori, D. Pinto, Y. Pivak, J. T. van Ommen, S. J. May, Y. Gogotsi, M. L. Taheri, *Nat. Commun.* **2019**, 10, 522.
- [19] A. Miranda, J. Halim, M. W. Barsoum, A. Lorke, *Appl. Phys. Lett.* **2016**, 108, 033102.
- [20] M. Hu, T. Hu, Z. Li, Y. Yang, R. Cheng, J. Yang, C. Cui, X. Wang, *ACS Nano* **2018**, 12, 3578.
- [21] K. L. Kaiser, *Electromagnetic Shielding*, Taylor and Francis, London **2005**.
- [22] R. Moore, *Electromagnetic Composites Handbook*, 2nd ed., McGraw-Hill Education, New York **2016**.
- [23] M. Born, E. Wolf, A. B. Bhatia, *Principles of Optics Electromagnetic Theory of Propagation, Interference and Diffraction of Light*, Cambridge University Press, Cambridge **2016**.
- [24] R. M. Simon, *Polym. Plast. Technol. Eng.* **1981**, 17, 1.
- [25] C. C. Katsidis, D. I. Siapkas, *Appl. Opt.* **2002**, 41, 3978.
- [26] B. Wen, M. Cao, M. Lu, W. Cao, H. Shi, J. Liu, X. Wang, H. Jin, X. Fang, W. Wang, J. Yuan, *Adv. Mater.* **2014**, 26, 3484.
- [27] M. Han, X. Yin, H. Wu, Z. Hou, C. Song, X. Li, L. Zhang, L. Cheng, *ACS Appl. Mater. Interfaces* **2016**, 8, 21011.
- [28] P. Kumar, F. Shahzad, S. Yu, S. M. Hong, Y.-H. Kim, C. M. Koo, *Carbon* **2015**, 94, 494.
- [29] V. Svorcik, J. Zehentner, V. Rybka, P. Slepicka, V. Hnatowicz, *Appl. Phys. A* **2002**, 75, 541.
- [30] D. Gall, *J. Appl. Phys.* **2016**, 119, 085101.
- [31] A. Akbari, P. Sheath, S. T. Martin, D. B. Shinde, M. Shaibani, P. C. Banerjee, R. Tkacz, D. Bhattacharyya, M. Majumder, *Nat. Commun.* **2016**, 7, 10891.
- [32] J. Zhong, W. Sun, Q. Wei, X. Qian, H.-M. Cheng, W. Ren, *Nat. Commun.* **2018**, 9, 3484.
- [33] T. Yun, J. S. Kim, J. Shim, D. S. Choi, K. E. Lee, S. H. Koo, I. Kim, H. J. Jung, H. W. Yoo, H. T. Jung, S. O. Kim, *ACS Appl. Mater. Interfaces* **2017**, 9, 1021.
- [34] S. J. Kim, J. Choi, K. Maleski, K. Hantanasirisakul, H.-T. Jung, Y. Gogotsi, C. W. Ahn, *ACS Appl. Mater. Interfaces* **2019**, 11, 32320.
- [35] S. H. Lee, S. Yu, F. Shahzad, W. N. Kim, C. Park, S. M. Hong, C. M. Koo, *Nanoscale* **2017**, 9, 13432.
- [36] Z. Li, Z. Wang, W. Lu, B. Hou, *Metals* **2018**, 8, 652.
- [37] J. Joo, C. Y. Lee, *J. Appl. Phys.* **2000**, 88, 513.
- [38] G. R. Fowles, *Introduction to Modern Optics*, Dover Publications **1989**.
- [39] W. T. Cao, F. F. Chen, Y. J. Zhu, Y. G. Zhang, Y. Y. Jiang, M. G. Ma, F. Chen, *ACS Nano* **2018**, 12, 4583.